Separation of Bones From Chest Radiographs by Means of Anatomically Specific Multiple Massive-Training ANNs Combined With Total Variation Minimization Smoothing

Sheng Chen* and Kenji Suzuki, *Senior Member, IEEE*

***Abstract*—Most lung nodules that are missed by radiologists as well as computer-aided detection (CADe) schemes overlap with ribs or clavicles in chest radiographs (CXRs). The purpose of this study was to separate bony structures such as ribs and clavicles from soft tissue in CXRs. To achieve this, we developed anatomically specific multiple massive-training artificial neural networks (MTANNs) combined with total variation (TV) minimization smoothing and a histogram-matching-based consistency improvement method. The anatomically specific multiple MTANNs were designed to separate bones from soft tissue in different anatomic segments of the lungs. Each of the MTANNs was trained with the corresponding anatomic segment in the teaching bone images. The output segmental images from the multiple MTANNs were merged to produce an entire bone image. TV minimization smoothing was applied to the bone image for reduction of noise while preserving edges. This bone image was then subtracted from the original CXR to produce a soft-tissue image where bones were separated out. This new method was compared with conventional MTANNs with a database of 110 CXRs with nodules. Our new anatomically specific MTANNs separated rib edges, ribs close to the lung wall, and the clavicles from soft tissue in CXRs to a substantially higher level than did the conventional MTANNs, while the conspicuity of lung nodules and vessels was maintained. Thus, our technique for bone–soft-tissue separation by means of our new MTANNs would be potentially useful for radiologists as well as CADe schemes in detection of lung nodules on CXRs.**

***Index Terms*—Chest radiography, computer-aided detection, lung nodules, pixel-based machine learning, virtual dual-energy.**

I. Introduction

THE PREVALENCE of chest diseases has been increasing over a long period of time. Every year, more than nine million people worldwide die from chest diseases [1]. Chest radiography (chest X-ray: CXR) is by far the most commonly used diagnostic imaging technique for identifying chest diseases such as lung cancer, tuberculosis, pneumonia, pneumoconioses, and pulmonary emphysema. This is because CXR is the most cost-effective, routinely available, and dose-effective diagnostic tool, and has the ability to reveal certain unsuspected pathologic alterations [2]. Among different chest diseases, lung cancer is responsible for more than 900 000 deaths each year, making it the leading cause of cancer-related deaths in the world. CXRs are regularly used for detecting lung cancer [3]–[5] as there is evidence that early detection of the tumor can result in a more favorable prognosis [6]–[8].

Although CXR is widely used for the detection of pulmonary nodules, the occurrence of false-negatives for nodules on CXRs is relatively high, and CXR is inferior to CT with respect to the detection of small nodules. This failure to detect nodules has been attributed to their size and density and to obscuring by structures such as ribs, clavicles, mediastinum, and pulmonary blood vessels. It has been well demonstrated that the detection of lung cancer at an early stage using CXRs is a very difficult task for radiologists. Studies have shown that up to 30% of nodules in CXRs could be missed by radiologists, and that 82%–95% of the missed nodules were partly obscured by overlying bones such as ribs and clavicles [9], [10]. However they would be relatively obvious on soft-tissue images if the dual-energy subtraction technique was used [11]. Therefore, a computer-aided detection (CADe) scheme [12], [13] for nodule detection on CXRs has been investigated because the computer prompts indicating nodules could improve radiologists' detection accuracy [14]–[16]. A major challenge for current CADe schemes is the detection of nodules overlapping with ribs, rib crossings, and clavicles, because the majority of false positives (FPs) are caused by these structures [17], [18]. This leads to a lower sensitivity as well as specificity of a CADe scheme. In order to overcome these challenges, Kido *et al.* developed a CADe scheme based on single-exposure dual-energy computed radiography [19], [20]. A dual-energy subtraction technique [21], [22] was used for separating soft tissue from bones in CXRs by use of two X-ray exposures at two different energy levels. The technique produces soft-tissue images from which bones are extracted. By using these images, the performance of their CADe scheme was improved. In spite of its great advantages, a limited number of hospitals use the dual-energy radi-

Manuscript received August 11, 2013; revised September 24, 2013; accepted September 25, 2013. Date of publication October 11, 2013; date of current version January 30, 2014. This work was supported in part by the Natural Science Foundation of China (NSFC) 81101116, and in part by Jiangsu Province Key Technology R&D Program BE2012630. *Asterisk indicates corresponding author.*

*S. Chen is with the University of Shanghai for Science and Technology, Shanghai 200093, China (e-mail: chnshn@hotmail.com).

K. Suzuki is with the Department of Radiology, University of Chicago, Chicago, IL 60637 USA.

Color versions of one or more of the figures in this paper are available online at http://ieeexplore.ieee.org.

Digital Object Identifier 10.1109/TMI.2013.2284016

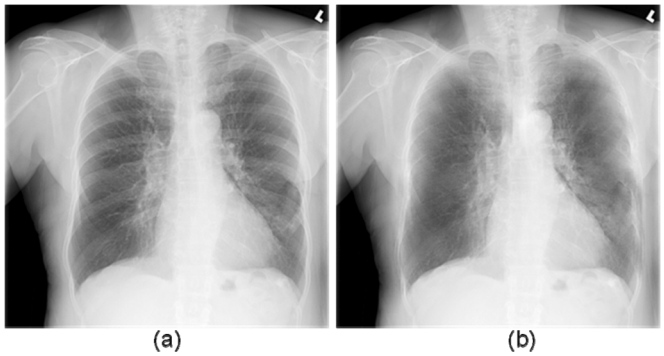

Fig. 1. Illustration of (a) an original standard chest radiograph and (b) the corresponding VDE soft-tissue image by use of our original MTANN method.

ography system because specialized equipment is required. In addition, the radiation dose can, in theory, be double compared to that for standard CXR.

Suzuki *et al.* first developed a supervised image-processing technique for separating ribs from soft tissue in CXRs by means of a multi-resolution massive-training artificial neural network (MTANN) [23], [24] which is a class of pixel-based machine learning [25] and is considered a supervised highly nonlinear filter based on artificial neural network regression. Real dual-energy images were used as teaching images for training of the multi-resolution MTANN. Once the multi-resolution MTANN was trained, real dual-energy images were no longer necessary. An observer performance study with 12 radiologists demonstrated that the suppression of bony structures in CXRs improved the diagnostic performance of radiologists in their detection of lung nodules substantially [26]. Ahmed *et al.* presented a technique based on independent component analysis for the suppression of posterior ribs and clavicles in order to enhance the visibility of nodules and to aid radiologists during the diagnosis process [27]. Loog *et al.* proposed a supervised filter learning technique for the suppression of ribs [28]. The procedure is based on K-nearest neighbor regression, which incorporates knowledge obtained from a training set of dual-energy radiographs with their corresponding subtraction images for the construction of a soft-tissue image from a previously unseen single standard chest image. The MTANN [23], [24] was able to separate ribs from soft tissue in CXRs; however, rib edges, ribs close to the lung wall, and clavicles were not completely suppressed (Fig. 1). The reason for this is that the orientation, width, contrast, and density of bones are different from location to location in the CXR, and the capability of a single set of multi-resolution MTANNs is limited.

The purpose of this study was to separate rib edges, ribs close to the lung wall, and clavicles from soft tissue in CXRs. To achieve this goal, we newly developed anatomically specific multiple MTANNs, each of which was designed to process the corresponding anatomic segment in the lungs. A composite virtual dual energy (VDE) bone image was formed from multiple output images of the anatomically specific multiple MTANNs by using anatomic segment masks, which were automatically segmented. In order to make the contrast and density of the output image of each set of MTANNs consistent, histogram matching was applied to process the training images. Before a

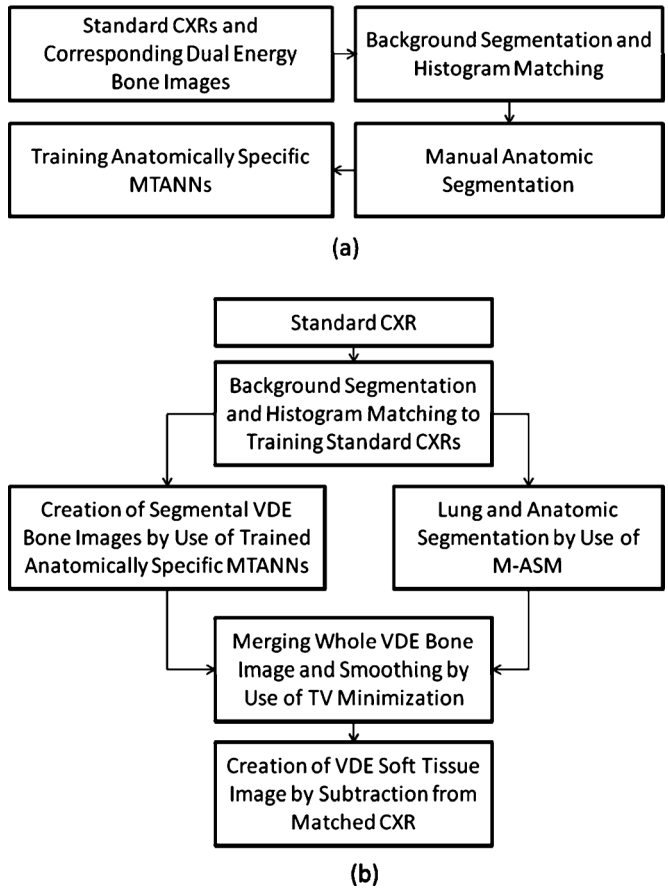

Fig. 2. Main diagram of our approach to bone separation from CXR. (a) Training phase. (b) Application phase.

VDE bone image was subtracted from the corresponding CXR to produce a VDE soft image, a total variation (TV) minimization smoothing method was applied to maintain rib edges. Fig. 2 shows the main diagram of our approach to bone separation from CXR. Our newly developed MTANNs were compared with our conventional MTANNs.

II. Materials and Method

A. Database of CXRs

The database used in this study consisted of 119 posterior–anterior CXRs acquired with a computed radiography (CR) system with a dual-energy subtraction unit (FCR 9501 ES; Fujifilm Medical Systems, Stamford, CT, USA) at The University of Chicago Medical Center. The dual-energy subtraction unit employed a single-shot dual-energy subtraction technique, where image acquisition is performed with a single exposure that is detected by two receptor plates separated by a filter for obtaining images at two different energy levels [29]–[31]. The CXRs included 118 abnormal cases with pulmonary nodules and a "normal" case (i.e., a nodule-free case). Among them, eight nodule cases and the normal case were used as a training set, and the rest were used as a test set. The matrix size of the chest images was 1760×1760 pixels (pixel size, 0.2 mm; gray scale, 10 bits). The absence and presence of nodules in the CXRs were confirmed through CT examinations. Most nodules overlapped with ribs and/or clavicles in CXRs.

B. Multi-Resolution MTANNs for Bone Suppression

For bone suppression, the MTANN [32] consisted of a machine-learning regression model such as a linear-output multilayer ANN regression model [33], which is capable of operating directly on pixel data. This model employs a linear function instead of a sigmoid function as the activation function of the unit in the output layer. This was used because the characteristics of an ANN have been shown to be significantly improved with a linear function when applied to the continuous mapping of values in image processing [33], [34]. Other machine-learning regression models can be used in the MTANN framework (also known as, pixel-based machine learning [25]) such as support vector regression and nonlinear Gaussian process regression models [35]. The output is a continuous value.

The MTANN involves training with massive sub-region-pixel pairs, which we call a massive-sub-regions training scheme. For bone suppression, CXRs are divided pixel by pixel into a large number of overlapping subregions (or image patches). Single pixels corresponding to the input subregions are extracted from the teaching images as teaching values. The MTANN is massively trained by using each of a large number of the input subregions (or patches) together with each of the corresponding teaching single pixels. The inputs to the MTANN are pixel values in a subregion (or an image patch), R extracted from an input image. The output of the MTANN is a continuous scalar value, which is associated with the center pixel in the subregion, represented by

$$O(x,y) = ML\{I(x-i, y-j) | (i,j) \in R\} \tag{1}$$

where $ML(\cdot)$ is the output of the machine-learning regression model, and $I(x,y)$ is a pixel value of the input image. The error to be minimized by training of the MTANN is represented by

$$E = \frac{1}{P} \sum_{c} \sum_{(x,y) \in R_T} \{T_c(x,y) - O_c(x,y)\}^2 \tag{2}$$

where c is the training case number, O_c is the output of the MTANN for the cth case, T_c is the teaching value for the MTANN for the cth case, and P is the number of total training pixels in the training region for the MTANN, R_T.

Bones such as ribs and clavicles in CXRs include various spatial-frequency components. For a single MTANN, suppression of ribs containing such variations is difficult, because the capability of a single MTANN is limited, i.e., the capability depends on the size of the subregion of the MTANN. In order to overcome this issue, multi-resolution decomposition/composition techniques were applied.

First, input CXRs and the corresponding teaching bone images were decomposed into sets of images of different resolution and these were then used for training three MTANNs in the multi-resolution MTANN. Each MTANN is an expert for a certain resolution, i.e., a low-resolution MTANN is responsible for low-frequency components of ribs, a medium-resolution MTANN is for medium-frequency components, and a high-resolution MTANN for high-frequency components. Each resolution MTANN is trained independently with the corresponding resolution images. After training, the MTANNs produce images of different resolution, and then these images are combined to provide a complete high-resolution image by use of the multi-resolution composition technique. The complete high-resolution image is expected to be similar to the teaching bone image; therefore, the multi-resolution MTANN would provide a VDE bone image in which ribs are separated from soft tissues.

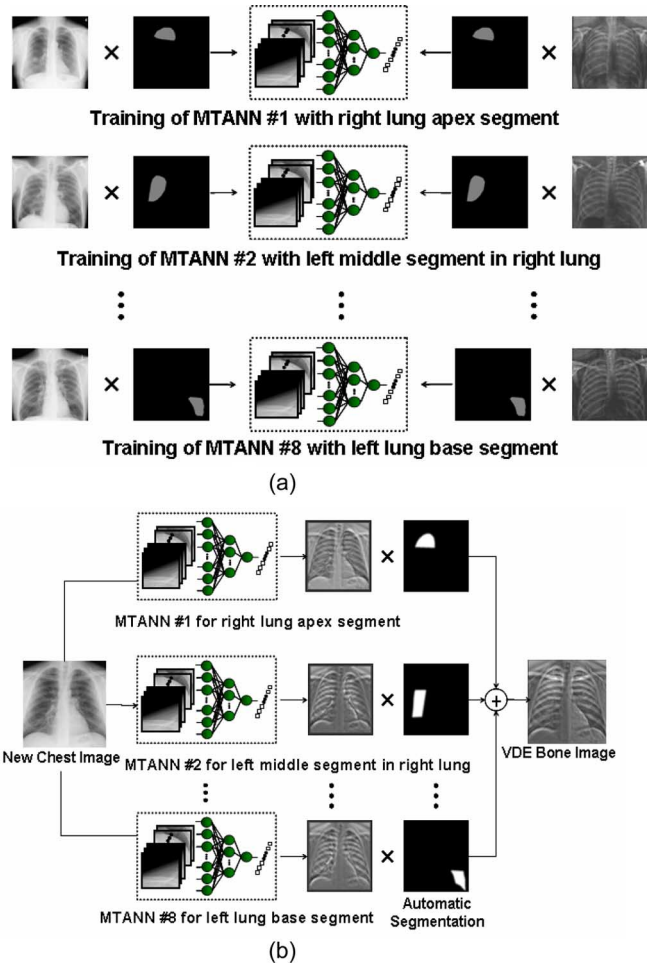

Fig. 3. Architecture and training of our new anatomically specific MTANNs. (a) Training phase. (b) Execution phase.

C. Anatomically Specific Multiple MTANNs

Although an MTANN was able to suppress ribs in CXRs [23], the single MTANN did not efficiently suppress rib edges, ribs close to the lung wall, and the clavicles, because the orientation, width, contrast, and density of bones are different from location to location, and because the capability of a single MTANN is limited. To improve the suppression of bones at different locations, we extended the capability of a single MTANN and developed an anatomically specific multiple-MTANN scheme that consisted of eight MTANNs arranged in parallel, as shown in Fig. 3(a). Each anatomically specific MTANN was trained independently by use of normal cases and nodule cases in which nodules were located in the corresponding anatomic segment. The lung field was divided into eight anatomic segments: a left upper segment for suppression of left clavicles and ribs, a left hilar segment for suppression of bone in the hilar area, a left

middle segment for suppression of ribs in the middle of the lung field, a left lower segment for suppression of ribs in the left lower lobe, a right upper segment, a right hilar segment, a right middle segment, and a right lower segment. For each anatomically specific MTANN, the training samples were extracted specifically from the corresponding anatomic segment mask [the training region in (2)]. The masks used in the training phase shown in Fig. 3(a) were segmented manually.

After training, each of the segments in a nontraining CXR was inputted into the corresponding trained anatomically specific MTANN for processing of the anatomic segment in the lung field, e.g., MTANNs No.1 was trained to process the left-upper segment in the lung field in which the clavicle lies; MTANNs No.2 was trained to process the left hilar segment, etc, as illustrated in Fig. 3(b). The eight segmental output sub-images from the anatomically specific multiple MTANNs were then composited to an entire VDE bone image by use of the eight anatomic segment masks. To blend the sub-images smoothly near their boundaries, anatomic segmentation masks smoothed by a Gaussian filter were used to composite the output sub-images, represented by

$$f_b(x,y) = \sum_{i=1}^{8} O_i(x,y) \times f_G[M_i(x,y)] \tag{3}$$

where $f_b(x,y)$ is the composite bone image, O_i is the ith trained anatomically specific MTANN, $f_G(\cdot)$ is a Gaussian filtering operator, and M_i is the ith anatomic segmentation mask. In our experiment, the parameter of sigma for the Gaussian filtering was determined to be 10.0 and the size of the template was 9×9 pixels.

D. Training Method

In order to make the output image of each set of anatomical segment MTANNs consistent in density and contrast, it is preferable to use similar CXRs to train each anatomical segment. A normal case was therefore selected for training the eight MTANNs with different segments of the lung field. In order to maintain nodule contrast while suppressing bone structures, nodules cases were used to train the anatomical segment specific multiple MTANNs as well. As it is impossible to find an abnormal case where each of eight typical nodules is located in each of the eight anatomical segments in the lung field, eight different nodule cases were required for training eight anatomical MTANNs. For each nodule case, a nodule was located in the anatomical segment that was used to train the corresponding MTANN. As a result, nine CXRs were used, i.e., one normal case and eight nodule cases, along with the corresponding dual-energy bone images for training the eight sets of multi-resolution MTANNs.

For training of overall features in each anatomic segment in the lung field, 10 000 pairs of training samples were extracted randomly from the anatomic segment for each anatomically specific MTANN: 5000 samples from the normal case; and 5000 samples from the corresponding nodule case. A three-layered MTANN was used, where the numbers of input, hidden, and output units were 81, 20, and 1, respectively. Once the MTANNs are trained, the dual-energy imaging system is no longer necessary. The trained MTANNs can be applied to standard CXRs for suppression of bones; thus the term "virtual dual-energy" (VDE) technology. The advantages of this technology over real dual-energy imaging are that there is no need for special equipment to produce dual-energy images, or no additional radiation dose to patients.

Because of differences in acquisition conditions and patients among different CXRs, the density and contrast vary within the different training images. This makes the training of the eight anatomically specific MTANNs inconsistent. To address this issue, a histogram-matching technique was applied to training images to equalize the density and contrast. Histogram matching is a technique for matching the histogram of a given image with that of a reference images. We used a normal case as the reference image to adjust the nodule cases. First, the cumulative histogram F_1 of the given image and that F_2 of the reference image were calculated. Then, the histogram transfer function $M(G_1) = G_2$ was calculated so that $F_1(G_1) = F_2(G_2)$. Finally, the histogram transfer function M was applied to each pixel in the given image.

The proportion of background also varies among different CXRs. The histogram matching of an image with a larger proportion of the background to another with a small proportion may cause the density of the lung field in the matched image to appear darker than the target image. For this reason, only the histogram of the body without the background was matched in the target image. The background was first segmented, which typically corresponds to the highest signal levels in the image where the unobstructed radiation hits the imaging plate. Several factors make the detection of these regions a challenging task. First, the radiation field across the image may be nonuniform due to the orientation of the X-ray source relative to the imaging plate, and the effect of scatter in thicker anatomical regions compounds this problem. Further, for some examinations, multiple exposures may be carried out on a single plate, resulting in multiple background levels. The noise attributes of the imaging system were used to determine if the variation around a candidate background pixel is a typical range of direct exposure pixel values. The corresponding values of candidate background pixels were accumulated in a histogram, and the resulting distribution of background pixel values invariably contained well-defined peaks, which served as markers for selecting the background threshold. The background peak was searched from low to high intensities in the smoothed histogram and detected as the first occurrence of a local maximum as follows:

$$\text{if } (\text{histogram}_{\text{smooth}}(i) > \text{histogram}_{\text{smooth}}(i + \Delta_{\text{step}}),$$
$$\text{then } \text{Peak}_{\text{background}} = i$$

where Δ_{step} was determined to be 8 bins in our experiment and

$$\text{histogram}_{\text{smooth}}(i) = \sum_{k=-2}^{2} \text{histogram}(i+k)/5.0.$$

After analyzing the histogram, the intensity values to the left of the background peak clearly represented the background, while those to the right represented, to a progressively greater extent, the intensity values of image information. The portion

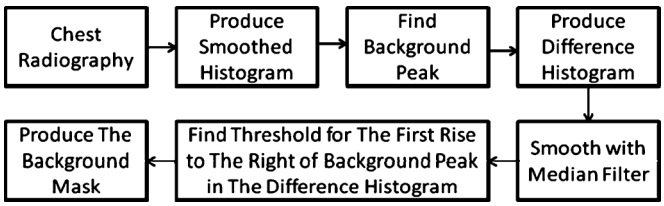

Fig. 4. Main diagram of background segmentation in CXR.

of the histogram to the right of the background peak was processed to find the point at which the histogram first exhibited a change in its curvature from negative to positive. For an increase in intensity, a negative curvature corresponds to a decreasing rate of occurrence of background pixels, while a positive curvature corresponds to an increasing rate of occurrence. In this manner, it was possible to create a difference histogram to obtain a positive slope at the intensity position to the right of the background peak. The difference histogram was smoothed with a five-bin median filter

$$\begin{aligned}&\mathrm{diff}(i) = \mathrm{histogram}_{\mathrm{smooth}}(i) - \mathrm{histogram}_{\mathrm{smooth}}(i-1)\\&\mathrm{diff}_{\mathrm{smooth}}(i) = \mathrm{median}(\mathrm{diff}(i-2), \mathrm{diff}(i-1)\\&\mathrm{diff}(i), \mathrm{diff}(i+1), \mathrm{diff}(i+2)).\end{aligned}$$

The best threshold intensity between background and signal was determined by finding the first Δ_{step} rise in the smoothed difference histogram to the right of the background peak, namely

$$\begin{aligned}&\text{if } (\mathrm{diff}_{\mathrm{smooth}}(i) < \mathrm{diff}_{\mathrm{smooth}}(i+\Delta_{\mathrm{step}}),\\&\text{then Threshold} = i.\end{aligned}$$

At this position, we could determine the counts for the least intense pixels, whose intensities are mostly due to the signal. After finding the intensity level representative of the minimum signal intensity level, this level was applied as a signal threshold for segmenting the background. This approach successfully dealt with the problems of nonuniform backgrounds. Fig. 4 shows the main diagram of background segmentation in CXR. Fig. 5 illustrates our background segmentation result. A background peak is seen in the histogram illustrated in Fig. 5(a). Fig. 5(b) illustrates a segmentation threshold determined by finding the first rise to the right of the background peak in the difference histogram. Fig. 5(d) shows the background segmentation result by using the threshold value.

E. Automated Anatomic Segmentation

To train and process anatomically specific MTANNs, a given CXR was divided into anatomic segments. Each segment was inputted into each of anatomically specific MTANNs simultaneously. Each MTANN provided the corresponding segment of a VDE bone image where bones were extracted. Because each MTANN is an expert for a specific anatomic segment, the signal-to-noise ratio is highest in the corresponding anatomic segment among all segments, as illustrated in Fig. 6. Merging all anatomic segments provided a complete single VDE bone image where the signal-to-noise ratio is high in all segments.

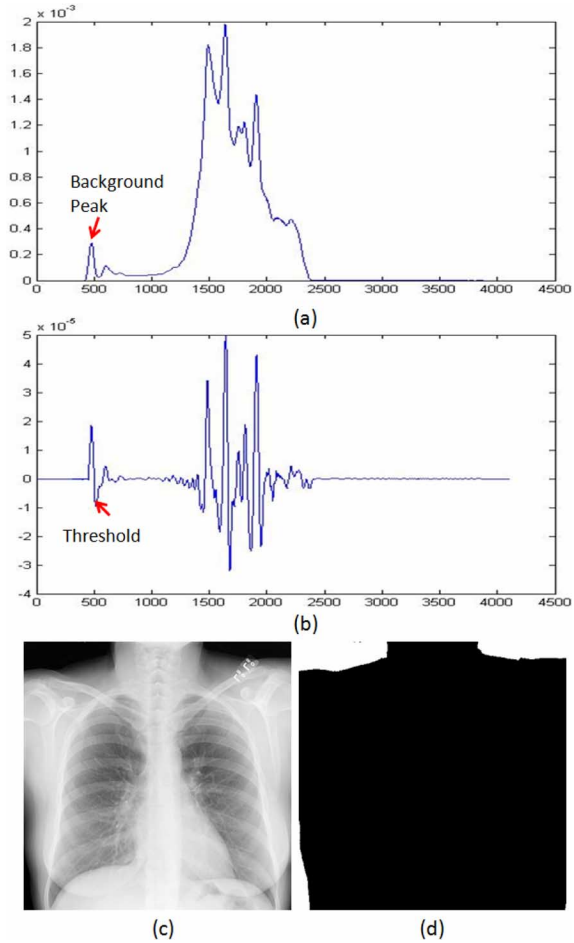

Fig. 5. Background segmentation. (a) Smoothed histogram of pixel values in CXR (b). (b) Differences between two neighboring bins in smoothed histogram (a). (c) Original CXR. (d) Background segmentation result.

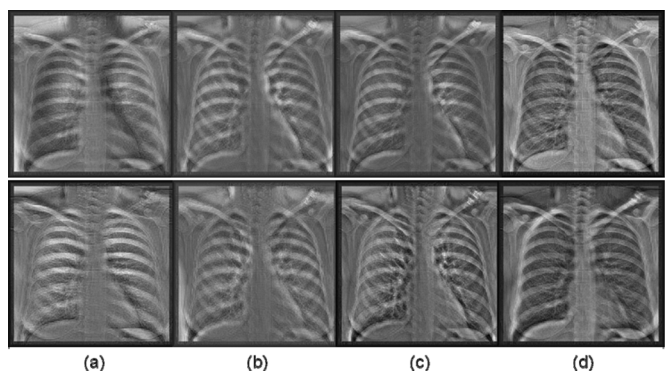

Fig. 6. Eight output bone images of the trained anatomically specific multiple MTANNs. (a) Output from the segment MTANNs trained for the hilar region. (b) Output from the MTANNs trained for the lower region of the lung. (c) Output from the MTANNs trained for the middle region of the lung. (d) Output from the MTANNs trained for the upper region of the lung.

To determine eight anatomic segments, an automated anatomic segmentation method was developed based on active shape models (ASMs) [36]. First, the lung fields were segmented automatically by using a multi-segment ASM (M-ASM) scheme [37], which can be adapted to each of the segments of the lung boundaries (which we call a multi-segment adaptation approach), as illustrated in Fig. 7. As the nodes

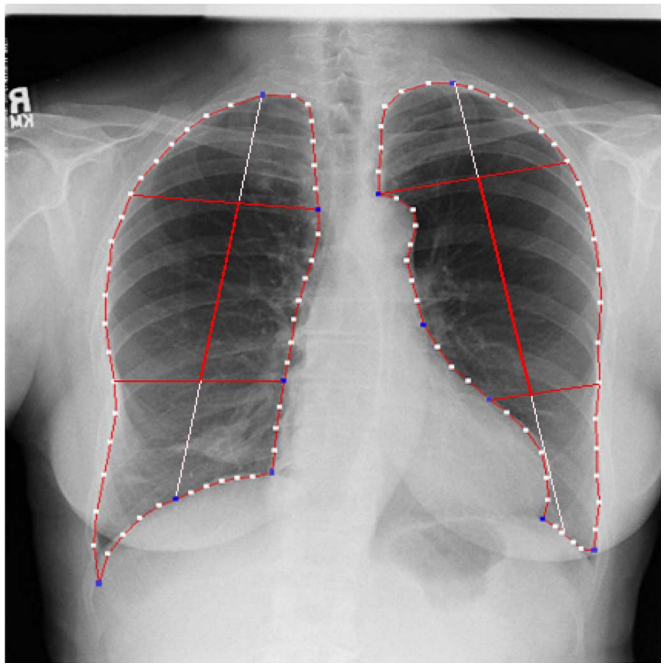

Fig. 7. Result of automated anatomic segmentation based on our M-ASM.

in the conventional ASM are equally spaced along the entire lung shape, they do not fit parts with high curvatures. In our developed method, the model was improved by the fixation of selected nodes at specific structural boundaries that we call transitional landmarks. Transitional landmarks identified the change from one boundary type (e.g., a boundary between the lung field and the heart) to another (e.g., a boundary between the lung field and the diaphragm). This resulted in multiple segmented lung field boundaries where each segment is correlated with a specific boundary type (heart, aorta, rib cage, diaphragm, etc.). The node-specific ASM was built by using a fixed set of equally spaced nodes for each boundary segment. Our lung M-ASM consisted of a total of 50 nodes for each lung boundary that were not equally spaced along the entire contour. A fixed number of nodes were assigned to each boundary segment, and they were equally spaced along each boundary (as shown in Fig. 7). For example, the boundary between the left lung field and the heart consisted of 11 points in every image, regardless of the actual extent of this boundary in the image (see Fig. 7). This allowed the local features of nodes to fit a specific boundary segment rather than the whole lung, resulting in a marked improvement in the accuracy of boundary segmentation. From the training images, the relative spatial relationships among the nodes in each boundary segment were learned in order to form the shape model. The nodes were arranged into a vector x and projected into the principal component shape space, represented by the following equation:

$$b = V^T(x - \bar{x}) \tag{4}$$

where $V = (V_1 V_2 \ldots V_M)$ is the matrix of the first M eigenvectors for the shape covariance matrix, and $b = (b_1 b_2 \ldots b_M)^T$ is a vector of shape coefficients for the primary axes. The shape coefficients were constrained to lie in a range $\pm m\sqrt{\lambda_i}$ to generate only a plausible shape and projected back to node coordinates, represented by:

$$x = \bar{x} + Vb \tag{5}$$

where m usually has a value between 2 and 3 [38], and was 2.5 in our experiment.

After the lungs were segmented, they were automatically divided into eight anatomic segments by using the boundary types and the transitional landmarks. By using the landmark points, we obtained the upper region, lower region, and hilar region in each lung, as illustrated in Fig. 7. The eight output segmental images from the multiple MTANNs were merged into a single VDE bone image

$$f_b(x,y) = \sum_{i=1}^{8} f_b^i(x,y) * m_b^i(x,y) \tag{6}$$

where $f_b^i(x,y)$ is the output image from the ith MTANN and $m_b^i(x,y)$ is the anatomic segment mask for the ith MTANN which has been smoothed by a Gaussian filter so that an unnatural discontinuity between anatomical segments in the merged image was eliminated. Our TV minimization smoothing was then applied to the entire composited VDE bone image.

F. Creation of Soft-Tissue Images

After the VDE bone image was obtained, the VDE soft image could be acquired by use of the subtraction technique. In this study, we focused on the suppression of ribs and clavicles in the lung field regions, because this is where most nodules overlap with bony structures. For processing only in the lungs, lung segmentation was used, and suppression was done only in the segmented lungs in the subtraction technique. After the segmentation, a Gaussian filter was applied for smoothing the edges of the segmented lung regions to create an image $m(x,y)$ for masking the outside of the lung regions. The masking image was normalized to have values from 0 to 1. For suppression of ribs in an original CXR, the VDE bone image $f_b(x,y)$ produced by the anatomically specific multiple MTANN was subtracted from the original CXR $g(x,y)$ with the masking image $m(x,y)$ as follows:

$$f_S(x,y) = g(x,y) - w_C \times f_b(x,y) \times m(x,y) \tag{7}$$

where w_C is a weighting parameter for determining the contrast of ribs. By changing the weighting parameter w_C, one can obtain processed CXR with different contrast of ribs and clavicles.

As mentioned above, owing to the noise in the VDE bone image, the Gaussian smooth method was applied. Although this can smooth the noise in the VDE bone image, it can also smooth the bone edges. As a result, the bone edges are preserved in the VDE soft image when subtracting the VDE bone image from the corresponding CXR. In this paper, we propose a TV minimization noise smoothing method which can smooth the noise in the VDE bone image while preserving the edge information of bones (Fig. 8). TV minimization problems were first introduced into the context of image smoothing by Rudin [39]. The main advantage of the TV formulation is the ability to preserve edges in the images. This is because of the piecewise smooth

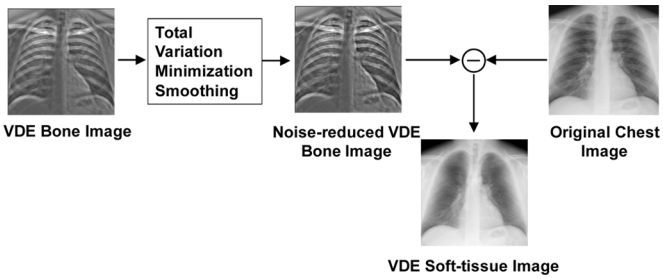

Fig. 8. Method for obtaining a soft-tissue image from a bone image.

regularization property of the TV norm. We assume the noise in the VDE bone image is white Gaussian noise

$$z(x,y) = u(x,y) + \eta(x,y) \tag{8}$$

where $u(x,y)$ is an unknown piecewise constant 2-D function representing the noise-free original image, $z(x,y)$ is the noisy observation of $u(x,y)$, and $\eta(x,y)$ is white Gaussian noise. A conventional additive noise suppression technique such as Wiener filtering was applied in order to find $u(x,y)$ which minimizes the functional

$$T(u) = \frac{1}{2}\|u-z\|^2 + \alpha J(u). \tag{9}$$

Common choices for J are

$$J(u) = \int u^2 dx. \tag{10}$$

Equation (9) often induces blur in images and spurious oscillations when u is discontinuous.

Therefore, we consider the nonlinear TV functional

$$J_{TV}(u) = \int_\Omega |\nabla u| dx \tag{11}$$

where ∇u denotes the gradient of u

$$\nabla u = \left(\frac{\partial u}{\partial x}, \frac{\partial u}{\partial y}\right).$$

Here, u is not required to be continuous.

However, the Euclidean norm is not differentiable at zero. To avoid difficulties associated with the nondifferentiability, the modification

$$J_\beta(u) = \int_\Omega \sqrt{|\nabla u|^2 + \beta^2} dx$$

will be utilized here, where β should be a very small value and was 0.0001 in our experiment.

The functional to be minimized is

$$T(u) = \frac{1}{2}\|u-z\|^2 + \alpha \int_\Omega \sqrt{|\nabla u|^2 + \beta^2}.dx \tag{12}$$

The Eular-lagrange equation associated with (12) is

$$\begin{aligned} u + \alpha L(u)u &= z, x \in \Omega \\ \frac{\partial u}{\partial n} &= 0, x \in \partial\Omega \end{aligned} \tag{13}$$

where $L(u)$ is a differential operator whose action on u is given by

$$L(u)u = -\nabla \cdot \left(\frac{1}{\sqrt{|\nabla u|^2 + \beta^2}} \nabla u\right). \tag{14}$$

It is an elliptic nonlinear partial differential equation (PDE). From (14), we can see that the smoothing decreases as the gradient strength increases, and the smoothing is stopped across edges.

There are many standard numerical optimization techniques such as conjugate gradient method. However, these standard methods tend to perform poorly on TV minimization problems. In this paper, we adopt the nonlinear multi-grid method to deal with this problem. Unlike the conventional methods, the multigrid algorithm can solve nonlinear elliptic PDE with nonconstant coefficients with hardly any loss in efficiency. In addition, no nonlinear equations need be solved, except on the coarsest grid.

Suppose we discrete the nonlinear elliptic PDE of (13) on a uniform grid with mesh size h

$$T_h(u_h) = z_h \tag{15}$$

where $T_h(u_h)$ denotes $u_h + \alpha L_h(u_h)u_h$.

Let $\tilde{u_h}$ denote some approximate solution and denote the exact solution to (15). Then the correction is

$$v_h = u_h - \tilde{u_h}.$$

The residual is

$$T_h(\tilde{u_h} + v_h) - T_h(\tilde{u_h}) = f_h - T_h(\tilde{u_h}) = -d_h. \tag{16}$$

Now, we form the appropriate approximation T_H of T_h on a coarser grid with mesh size H (we will always take $H = 2h$). The residual equation is now approximated by

$$T_H(u_H) - T_H(\tilde{u_H}) = -d_H. \tag{17}$$

Since T_H has smaller dimension, this equation will be easier to solve. To define $\tilde{u_H}$ and d_H on the coarse grid, we need a restriction operator H that restricts $\tilde{u_h}$ and d_h to the coarse grid. That is, we solve

$$T_H(u_H) = T_H(R\tilde{u_h}) - Rd_h \tag{18}$$

on the coarse gird. Then the coarse-grid correction is

$$\tilde{v_H} = u_H - R\tilde{u_h}.$$

Once we have a solution $\tilde{v_H}$ on the coarse gird, we need a prolongation operator P that interpolates the correction to the fine gird

$$\tilde{v_h} = P\tilde{v_H}.$$

So we have

$$\tilde{u_h}^{\text{new}} = \tilde{u_h} + P\tilde{v_H}. \tag{19}$$

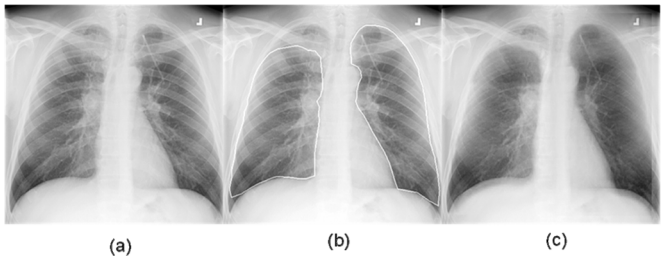

Fig. 9. Illustration of incomplete suppression caused by a lung segmentation failure (a) an original image, (b) lung field segmentation, and (c) bone suppression within the segmented lung fields. The right clavicle in (c) is not suppressed.

It is the two-grid algorithm and can be easily extended to multi-grid.

At the coarsest-grid, we have one remaining task before implementing our nonlinear multi-grid algorithm: choosing a nonlinear relaxation scheme. Our first choice is the nonlinear Gauss–Seidel scheme. If the discretized (15) is written with some choice of ordering as

$$T_i(u_1, \ldots, u_N) = z_i, i = 1, \ldots, N \tag{20}$$

then the nonlinear Gauss–Seidel scheme solves

$$T_i(u_1, \ldots, u_{i-1}, u_i^{\text{new}}, u_{i+1}, \ldots, u_N) = z_i$$

for u_i^{new}. Often the equation is linear in u_i^{new}, since the nonlinear terms are discretized by means of its neighbors. If this is not the case, we replace (20) by one step of a Newton iteration

$$u_i^{\text{new}} = u_i^{\text{old}} - \frac{T_i(u_i^{\text{old}}) - z_i}{\partial T_i(u_i^{\text{old}})/\partial u_i}. \tag{21}$$

III. Results

A. Lung Field and Anatomic Segment

Accurate background segmentation is prerequisite for histogram matching for consistency improvement. Because we did not have the background truth with which to compare segmentation results, we performed the visual evaluation of the background segmentation results for the 118 cases in our experiment, and found that they were all acceptable, i.e., there was no significant over- or under-segmentation.

Lung segmentation plays an important role in the bone suppression in this study. Inaccurate segmentation means that the anatomical segment mask will not correspond to the region mask trained in the anatomically specific multiple MTANNs. As a result, the bone structures will not be suppressed in the VDE soft image. Fig. 9 shows a failed case due to inaccurate segmentation of the lung field. It can be seen that some of the bones are suppressed whereas the clavicles are not. When the lung field was manually segmented into the eight anatomical segments, the clavicles were suppressed much more successfully than when the automatic segmentation was used.

In this study, 93 normal images from the public Japanese Society of Radiology Technique (JSRT) database were used for training of the M-ASM. The segmentation accuracy was computed by use of the overlap measure Ω

$$\Omega = \frac{TP_{\text{seg}}}{TP_{\text{seg}} + FP_{\text{seg}} + FN_{\text{seg}}} \tag{22}$$

where TP_{seg} was the area correctly classified as a lung field, FP_{seg} was the area incorrectly classified as a lung field, and FN_{seg} was the area incorrectly classified as the background. The mean and standard deviation of the overlap measure for all the 154 nodule images in the JSRT database were 0.913 and 0.023, respectively. For the 118 cases, because we do not have the lung field truth with which to compare our M-ASM segmentation results, we only give a visualization evaluation for the segmentation. In ten cases, the segmentation results were not as good as the other cases, i.e., there were relatively larger over- or under-segmentations. This may be because the M-ASM was trained by the normal cases from JSRT database, which are digitized images from film, whereas the U of C database consists of digital radiographs from a CR system. The performance of lung segmentation has the potential to be improved in our future work. These 10 bad segmentation cases were kept using in the subsequent bone separation steps in our approach.

In these experiments, 50 points for each M-ASM for each lung were applied and the relative position of each point in the segmentation results is known. The seventh point in the segment boundary between the lung field and the lung wall beginning from the apex of lung (the translating blue point), and the aortic arch blue point were used to achieve the upper lung segment. The sixth point beginning from costophrenic angle (blue point in the lowest position) and the blue point in the ventricle border were used to segment the lower lung region. Finally, the apex point and the blue point in the hemidiaphragm were used to segment the middle region to get the hilar region.

As a result, we can automatically obtain the anatomic segment based on the lung field segmentation results (Fig. 7).

B. Smoothing for VDE Bone Image

In order to prove the effectiveness of the TV minimization smoothing method, we applied a number of different methods to smooth the VDE bone image. Fig. 10(d) shows that the edges of the ribs are eliminated, as well as the other bone structures in the soft-like image, while the edges in Fig. 10(c), where the Gaussian smoothing method was used, were more obvious.

In our experiment, the smoothing parameter used for the original VDE bone image was usually larger than that of the improved VDE bone image. The reason is that in our improved bone suppression method, each set of anatomic specific MTANNs only process a single anatomic segment with a simple pattern. The signal to noise ratio is higher than that for the whole lung field. When the original VDE bone image and the improved VDE bone images were subtracted from the original CXR without any smoothing, the improved VDE soft tissue image was seen to be better than the original VDE soft image.

Compared to the Gaussian smoothing method, the processing time of TV minimization is only 1 s per case because of the multi-grad algorithm applied in this experiment.

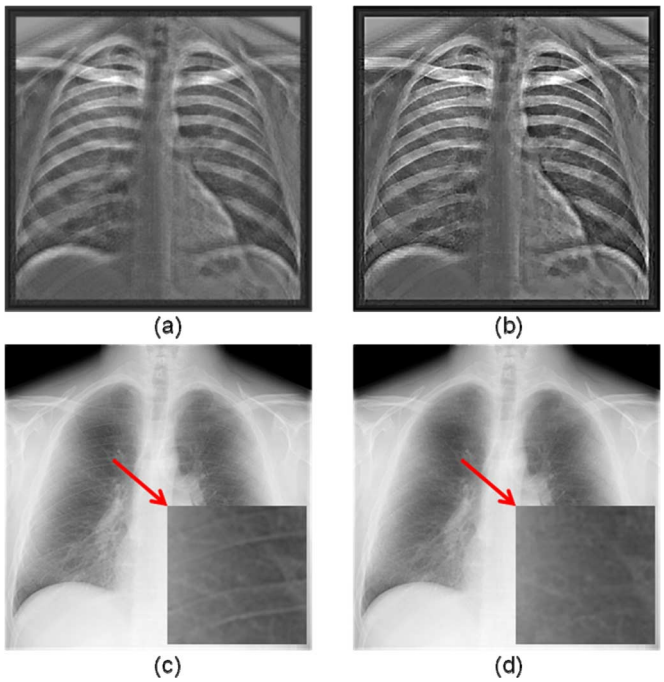

Fig. 10. Illustration of (a) a VDE bone image with Gaussian smoothing, (b) a VDE bone image with TV-minimization-based smoothing, (c) a VDE soft-tissue image corresponding to (a), and (d) a VDE soft-tissue image corresponding to (b), all by use of the anatomically specific multiple MTANNs.

C. Evaluation

The newly developed anatomically specific multiple MTANNs were subjected to a validation test that included 110 nodule cases. The bone suppression performance was quantitatively evaluated by using the absolute error [4], represented by

$$E_N = \sum_{x,y \in R_L} |b(x,y) - f_b(x,y)| / N_L (b_{\max} - b_{\min}) \tag{23}$$

where $f_b(x,y)$ is the VDE bone image, $b(x,y)$ is the corresponding "gold-standard" dual-energy bone image, R_L indicates lung regions, N_L is the number of pixels in R_L, and $b_{\max}$ and $b_{\min}$ are the maximum value and the minimum value in R_L in the dual-energy bone image, respectively. The result for the 110 CXRs was an average E_N of 0.072 with a standard deviation of 0.012; both values are lower than our previous results [23] at a statistically significant level $(\mathrm{P} < 0.05)$.

Fig. 11 illustrates the results of bone suppression for a normal case. Compare to the old VDE soft-tissue images obtained by use of our conventional technique, rib edges, the clavicles, and ribs close to the lung wall are suppressed substantially, while the visibility of soft tissue such as vessels is maintained. The quality of the VDE soft-tissue images is comparable to that of the "gold-standard" dual-energy soft-tissue images.

Fig. 12 illustrates the results for a case where the nodule not only overlapped with ribs but was also close to the lung wall. In our previous method, the ribs close to the lung wall were not successfully suppressed and the contrast of the nodules in this area was similar to the original CXR. In the present improved method, the nodule was maintained while the surrounding ribs were suppressed, and the boundary of the nodule was clearer than that in the original CXR. Fig. 13 illustrates a case in which the nodule partly overlapped with bone. In our original results, the boundaries of the nodule were smoothed and the contrast of the nodule was partly suppressed. While in the improved result, there were clear nodule boundaries and the contrast of the nodule was close to that of the soft images. Fig. 14 illustrates a case of good preservation of nodule found in the left lung. Fig. 15 illustrates a case where the nodule was located in the hilar region. Both the contrast and shapes of the nodules were maintained very well using the present improved method compared to the original method where the nodules appeared diffuse with smoothed boundaries.

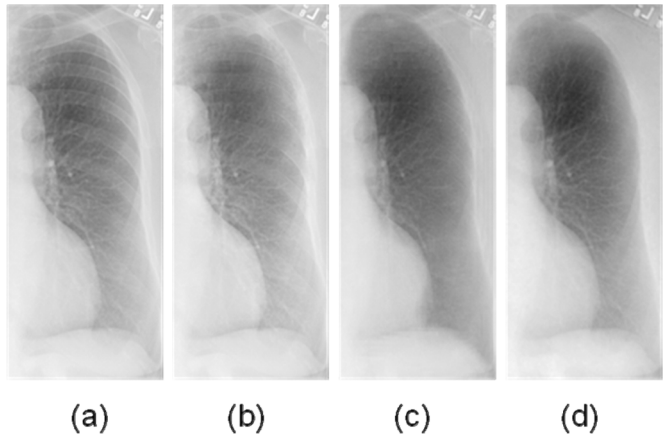

Fig. 11. Result for a nontraining normal chest radiograph. (a) An original normal chest radiograph, (b) a VDE soft-tissue image obtained by use of our original MTANN technique, (c) a VDE soft-tissue image obtained by use of our new MTANN technique, and (d) the corresponding "gold-standard" dual-energy soft-tissue image.

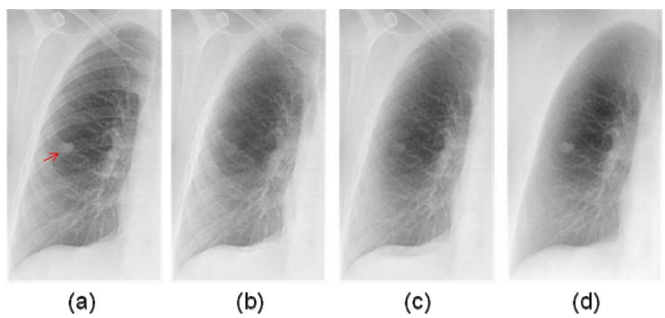

Fig. 12. Result for an abnormal chest radiograph with a nodule that overlaps with both anterior and posterior ribs. (a) An original abnormal chest radiograph with a nodule (indicated by a red arrow), (b) a VDE soft-tissue image obtained by use of our original MTANN technique, (c) a VDE soft-tissue image obtained by use of our new MTANN technique, and (d) the corresponding "gold-standard" dual-energy soft-tissue image.

IV. Discussion

In CXR, many nodules are overlapped with ribs, which are usually close to the lung wall, causing a large number of FPs in the CADe scheme. In previously described method, the posterior ribs were suppressed well but the anterior ribs were not suppressed sufficiently. From the VDE bone images, it can be seen that the nodules are still overlapped with the anterior ribs, which usually have a similar density to the nodule.

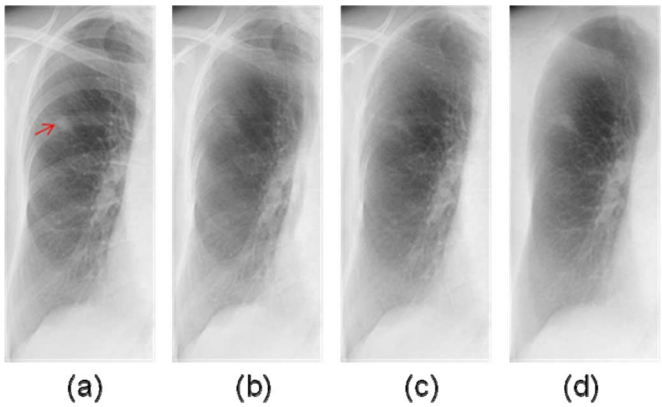

Fig. 13. Results for abnormal chest radiographs with a nodule that is mostly overlap with a rib. (a) An original abnormal chest radiograph with a nodule (indicated by a red arrow), (b) a VDE soft-tissue image obtained by use of our original MTANN technique, (c) a VDE soft-tissue image obtained by use of our new MTANN technique, and (d) the corresponding "gold-standard" dual-energy soft-tissue image.

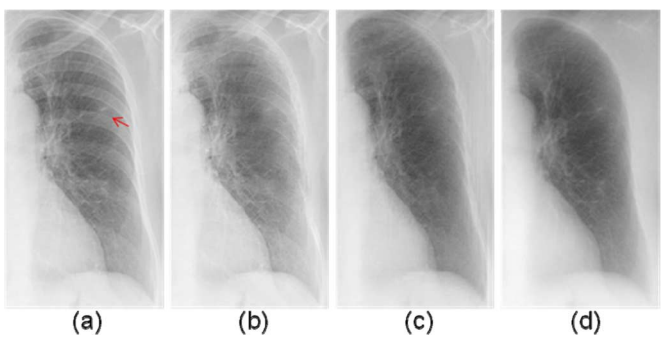

Fig. 14. Results for abnormal chest radiographs with a tiny nodule in the left lung. (a) An original abnormal chest radiograph with a nodule (indicated by a red arrow), (b) a VDE soft-tissue image obtained by use of our original MTANN technique, (c) a VDE soft-tissue image obtained by use of our new MTANN technique, and (d) the corresponding "gold-standard" dual-energy soft-tissue image.

All the results in this paper were achieved using the same parameters. However, we can optimize the suppression by use of different parameters for CXRs obtained using different exposure setting.

Although consistent processing was used on the training images to make the output images of each of the anatomic segment MTANNs in the bone suppression phase uniform, in some cases, there were still some differences between different anatomic segments in terms of the bone contrast and density. As a result, in some anatomical segments, the bone was not suppressed as well as in others. This may be because the bone contrast and density were more variable than in the images that were used for training.

One of the advantages of the M-ASM segmentation method used in this work is that it is possible to know which point belongs to which type of boundary and which point is the translation point in the contour of the segmentation. Based on these points, the lung field can be automatically divided into segments based on the anatomy. It is helpful to suppress the bones in different anatomical segments automatically.

In this study, we assume that the noise model in the VDE bone image is Gaussian, and the TV-based models can answer

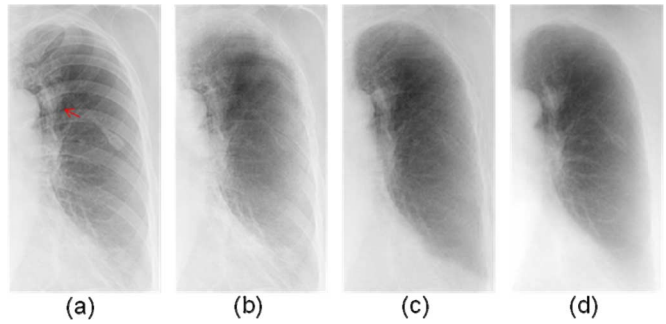

Fig. 15. Results for abnormal chest radiographs with a nodule in the hilar region of the lung. (a) An original abnormal chest radiograph with a nodule (indicated by a red arrow), (b) a VDE soft-tissue image obtained by use of our original MTANN technique, (c) a VDE soft-tissue image obtained by use of our new MTANN technique, and (d) the corresponding "gold-standard" dual-energy soft-tissue image.

fundamental questions arising in image restoration better than other models.

In our original method, only the posterior ribs were present in the VDE bone images. Owing to the anatomically specific multiple MTANNs used in this work, the anterior ribs were also present in the new VDE bone images. As the anterior ribs in a CXR are usually close to the lung wall, their suppression using this novel method was seen to be significantly better than using the original method.

Although nine cases were used (one normal, eight abnormal) for training the anatomically specific multiple MTANNs, only one normal case and one nodule case were used for each anatomic segment; however, the MTANNs produced reliable results for nontraining cases. A multi-resolution MTANN would be more robust against variations among cases if a larger number of cases were used for training.

MTANNs is a class of pixel/patch-based machine learning [25] that uses pixel values in a subregion (image patch) as the input information to a machine learning regression model, instead of features calculated from segmented objects in ordinary feature-based machine learning (or simply a classifier). Pixel/patch-based machine learning outputs pixel values, whereas feature-based machine learning such as a support vector machine classifier outputs classes such as normal or abnormal. The MTANN used in our bone separation technique employs an artificial neural network (ANN) regression model as the core machine learning regression, but other machine learning regression models can be used in the massive-training framework. We replaced the ANN regression model with support vector regression (SVR) and nonlinear Gaussian process regression (GPR) models in the massive-training framework, which are called MTSVR and MTGPR, respectively [35]. We performed experiments to figure out the advantages and disadvantages of MTANNs over the MTSVR and MTGPR in distinction between lesions (i.e., colonic polyps) and nonlesions in medical images (i.e., CT). A major disadvantage of the MTANN is the long training time because of the slow convergence property of the ANN model. Unlike the ANN model, the SVR and GPR models are memory-based methods that store a part of or the entire training data. Therefore, their training is generally fast. In our experiment, the MTSVR with a

Gaussian kernel and MTGPR were able to offer a performance comparable to that of the MTANN, with highly and better efficient training: the MTSVR and MTGPR yielded a reduction in the training time (from 38 h to 12 min and 25 h, respectively) by factors of 190 and 1.3. However, the execution time of the MTSVR and MTGPR are substantially longer than that of the MTANN because of the nature of the memory-based models. We expect the same properties describe above when we use the MTSVR and MTGPR in our bone separation technique. Namely, the performance on bone separation of the MTANN would be comparable to that of the MTSVR and MTGPR. The advantage of the use of the MTANN is a short execution time (i.e., 1.63 s. per image); its disadvantage is a long training time (e.g., 13 h).

As the use of a multi-resolution MTANN requires only software, this technique can be utilized on an existing viewing workstation. Although we applied a TV minimization based smoothing method, the processing time for creating a VDE soft image and a VDE bone image from a CXR is very short, i.e., 1.63 s on a PC-based workstation (CPU: Intel Pentium IV, 3.2 GHz) because the multi-grid solving method was used; thus, the software can be applied prior to interpretation in every case without incurring any delay.

As the fine structures of soft tissues, such as small vessels, are mostly maintained in the VDE soft tissue images, these images could potentially be used for quantitative assessment of interstitial lung diseases that are characterized by fine patterns. In addition, this technique could easily be applied to anatomic regions other than the lungs using dual-energy images training of the specific anatomic segments involved.

V. Conclusion

We have developed an anatomically specific multiple MTANN scheme to suppress bony structures in CXRs. With our new technique, rib edges, ribs close to the lung wall, and the clavicles were suppressed substantially better than was possible with our conventional technique, while soft tissue such as lung nodules and vessels was maintained. Thus, our technique would be useful for radiologists as well as for CADe schemes in the detection of lung nodules in CXRs.

Acknowledgment

The authors would like to thank H. MacMahon, MD, for his valuable clinical suggestions. Initial bone suppression technology and source code have been nonexclusively licensed to Riverain Medical (Riverain Technologies).

References

[1] C. J. Murray and A. D. Lopez, "Mortality by cause for eight regions of the world: Global burden of disease study," *Lancet*, vol. 349, pp. 1269–1276, May 3, 1997.

[2] G. P. Murphy *et al.*, American Cancer Society Textbook of Clinical Oncology2nd ed. Atlanta, GA, 1995.

[3] J. K. Frost *et al.*, "Early lung cancer detection: Results of the initial (prevalence) radiologic and cytologic screening in the Johns Hopkins study," *Am. Rev. Respirat. Disease*, vol. 130, pp. 549–554, Oct. 1984.

[4] R. S. Fontana *et al.*, "Early lung cancer detection: Results of the initial (prevalence) radiologic and cytologic screening in the Mayo Clinic study," *Am. Rev. Respirat. Disease*, vol. 130, pp. 561–565, Oct. 1984.

[5] C. I. Henschke *et al.*, "Radiographic screening for cancer. Proposed paradigm for requisite research," *Clin. Imag.*, vol. 18, pp. 16–20, Jan. –Mar. 1994.

[6] R. T. Heelan *et al.*, "Non-small-cell lung cancer: Results of the New York screening program," *Radiology*, vol. 151, pp. 289–293, May 1984.

[7] T. Sobue *et al.*, "Survival for clinical stage I lung cancer not surgically treated. Comparison between screen-detected and symptom-detected cases. The Japanese lung cancer screening research group," *Cancer*, vol. 69, pp. 685–692, Feb. 1, 1992.

[8] B. J. Flehinger *et al.*, "The effect of surgical treatment on survival from early lung cancer. Implications for screening," *Chest*, vol. 101, pp. 1013–1018, Apr. 1992.

[9] J. H. Austin *et al.*, "Missed bronchogenic carcinoma: Radiographic findings in 27 patients with a potentially resectable lesion evident in retrospect," *Radiology*, vol. 182, pp. 115–122, Jan. 1992.

[10] P. K. Shah *et al.*, "Missed non-small cell lung cancer: Radiographic findings of potentially resectable lesions evident only in retrospect," *Radiology*, vol. 226, pp. 235–241, Jan. 2003.

[11] F. Li *et al.*, "Improved detection of small lung cancers with dual-energy subtraction chest radiography," *AJR Am. J. Roentgenol.*, vol. 190, pp. 886–91, Apr. 2008.

[12] M. L. Giger *et al.*, "Image feature analysis and computer-aided diagnosis in digital radiography. 3. Automated detection of nodules in peripheral lung fields," *Med. Phys.*, vol. 15, pp. 158–166, Mar.–Apr. 1988.

[13] B. van Ginneken *et al.*, "Computer-aided diagnosis in chest radiography: A survey," *IEEE Trans. Med. Imag.*, vol. 20, no. 12, pp. 1228–1241, Dec. 2001.

[14] K. Abe *et al.*, "Computer-aided diagnosis in chest radiography. Preliminary experience," *Invest. Radiol.*, vol. 28, pp. 987–993, Nov. 1993.

[15] T. Kobayashi *et al.*, "Effect of a computer-aided diagnosis scheme on radiologists' performance in detection of lung nodules on radiographs," *Radiology*, vol. 199, pp. 843–848, Jun. 1996.

[16] S. Kakeda *et al.*, "Improved detection of lung nodules on chest radiographs using a commercial computer-aided diagnosis system," *AJR Am. J. Roentgenol.*, vol. 182, pp. 505–10, Feb. 2004.

[17] T. Matsumoto *et al.*, "Image feature analysis of false-positive diagnoses produced by automated detection of lung nodules," *Invest. Radiol.*, vol. 27, pp. 587–597, Aug. 1992.

[18] X. W. Xu *et al.*, "Development of an improved CAD scheme for automated detection of lung nodules in digital chest images," *Med. Phys.*, vol. 24, pp. 1395–1403, Sep. 1997.

[19] S. Kido *et al.*, "Detection of simulated pulmonary nodules by single-exposure dual-energy computed radiography of the chest: Effect of a computer-aided diagnosis system (Part 2)," *Eur. J. Radiol.*, vol. 44, pp. 205–9, Dec. 2002.

[20] S. Kido *et al.*, "Computerized detection of pulmonary nodules by single-exposure dual-energy computed radiography of the chest (Part 1)," *Eur. J. Radiol.*, vol. 44, pp. 198–204, Dec. 2002.

[21] R. Glocker and W. Frohnmayer, "Uber die rontgenspektroskopische Bestimmung des Gewichtsanteiles eines elementes in gememgen und verbindungen," *Annalen der Physik*, vol. 76, pp. 369–395, 1925.

[22] B. Jacobson and R. S. Mackay, "Radiological contrast enhancing methods," *Adv. Biol. Med. Phys.*, vol. 6, pp. 201–261, 1958.

[23] K. Suzuki *et al.*, "Image-processing technique for suppressing ribs in chest radiographs by means of massive training artificial neural network (MTANN)," *IEEE Trans. Med. Imag.*, vol. 25, pp. 406–416, Apr. 2006.

[24] K. Suzuki *et al.*, "Suppression of the contrast of ribs in chest radiographs by means of massive training artificial neural network," in *Proc. SPIE Med. Imag.*, San Diego, CA, 2004, pp. 1109–1119.

[25] K. Suzuki, "Pixel-based machine learning in medical imaging," *Int. J. Biomed. Imag.*, vol. 2012, p. 18, 2012.

[26] S. Oda *et al.*, "Performance of radiologists in detection of small pulmonary nodules on chest radiographs: Effect of rib suppression with a massive-training artificial neural network," *AJR Am. J. Roentgenol.*, vol. 193, pp. W397–W402, Nov. 2009.

[27] B. Ahmed and T. Rasheed, "Rib suppression for enhancing frontal chest radiographs using independent component analysis," *Lecture Notes in Computer Science*, vol. 4432, 2007.

[28] M. Loog *et al.*, "Filter learning: Application to suppression of bony structures from chest radiographs," *Med. Image Anal.*, vol. 10, pp. 826–40, Dec. 2006.

[29] T. Ishigaki *et al.*, "One-shot dual-energy subtraction imaging," *Radiology*, vol. 161, pp. 271–273, Oct. 1986.

[30] T. Ishigaki *et al.*, "One-shot dual-energy subtraction chest imaging with computed radiography: Clinical evaluation of film images," *Radiology*, vol. 168, pp. 67–72, July 1988.
[31] B. K. Stewart and H. K. Huang, "Single-exposure dual-energy computed radiography," *Med. Phys.*, vol. 17, pp. 866–875, Sep.–Oct. 1990.
[32] K. Suzuki *et al.*, "Massive training artificial neural network (MTANN) for reduction of false positives in compterized detection of lung nodules in low-dose CT," *Med. Phys.*, vol. 30, p. 15, 2003.
[33] K. Suzuki *et al.*, "Recognition of coronary arterial stenosis using neural network on DSA system," *Syst. Comput. Japan*, vol. 26, pp. 66–74, Aug. 1995.
[34] K. Suzuki *et al.*, "Neural edge enhancer for supervised edge enhancement from noisy images," *IEEE Trans. Pattern Anal. Mach. Intell.*, vol. 25, no. 12, pp. 1582–1596, Dec. 2003.
[35] J. Xu and K. Suzuki, "Massive-training support vector regression and Gaussian process for false-positive reduction in computer-aided detection of polyps in CT colonography," *Med. Phys.*, vol. 38, p. 14, 2011.
[36] B. van Ginneken *et al.*, "Segmentation of anatomical structures in chest radiographs using supervised methods: A comparative study on a public database," *Med. Image Anal.*, vol. 10, pp. 19–40, Feb. 2006.
[37] S. Chen *et al.*, "Development and evaluation of a computer-aided diagnostic scheme for lung nodule detection in chest radiographs by means of two-stage nodule enhancement with support vector classification," *Med. Phys.*, vol. 38, p. 15, 2011.
[38] B. van Ginneken *et al.*, "Active shape model segmentation with optimal features," *IEEE Trans. Med. Imag.*, vol. 21, no. 8, pp. 924–933, Aug. 2002.
[39] L. I. Rudin *et al.*, "Nonlinear total variation based noise removal algorithms," *Phys. D*, vol. 60, 1999.